Polymer Testing 128 (2023) 108232

Contents lists available at ScienceDirect

Polymer Testing

journal homepage: www.elsevier.com/locate/polytest

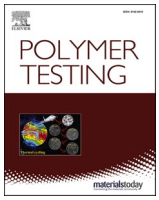

Low dose electron tomography of novel nanocomposites for additive manufacturing

M. Herrera [a,*], J. Hernández-Saz [b], N. Fernández-Delgado [a], L.M. Valencia [a], S.I. Molina [a]

[a] Departamento de Ciencia de los Materiales, I. M. y Q. I., IMEYMAT, Facultad de Ciencias, Universidad de Cádiz, Campus Río San Pedro, s/n, Puerto Real, Cádiz, 11510, Spain
[b] Departamento de Ingeniería y Ciencia de los Materiales y del Transporte, Universidad de Sevilla, Avda. Camino de los Descubrimientos s/n., Sevilla, 41092, Spain

ARTICLE INFO

Keywords:
Electron tomography
Low electron dose
Focused ion beam equipment
Nanocomposites
Additive manufacturing
Stereolithography

ABSTRACT

The development of new nanocomposites with added functionalities for Additive Manufacturing (AM) requires of a deep understanding of the 3D distribution of the selected nano-additives within the polymeric matrix, in order to optimize their performance. For this, electron tomography (ET) is an outstanding analysis technique that requires the material to withstand the electron exposure needed for the acquisition of several tens of images, becoming challenging for beam-sensitive materials. In this work, we analyse the parameters involved in the successful analysis by low dose ET of nanocomposites based in acrylic resins for stereolithography (SLA). Needle-shape electron-transparent specimens have been fabricated by focused ion beam (FIB), minimizing surface damage due to the high energy Ga^+ ions. Microscope settings for tuning the electron dose applied during the ET analysis of these nanoneedles are discussed. A phenomenological study of the effect of increasing the electron dose in the scanning transmission electron microscopy (STEM) analysis of the material has been carried out, showing that ET can be effectively performed at low electron doses. Two case studies are presented, to illustrate the relevance of these analyses in the development of nanocomposites with added functionalities. Our results have revealed the crucial role of the dose rate and of inaccuracies in the calculation of critical electron doses for the design of ET experiments.

1. Introduction

Additive manufacturing (AM) technologies are based in the layer-by-layer fabrication of 3D models created with computer-aided design (CAD), using a variety of equipment that can process materials such as polymers, metals or ceramics [1,2]. The versatility of AM technologies allows obtaining pieces with very complex geometries useful, for example, in parts with intricate internal features, or in lightweight pieces with hollow or lattice structures. Additional advantages of AM are competitive cost production, drastic reduction of waste and easy scalability [3]. Because of these potential benefits, AM has acquired an essential role in industry in the last decade, especially within Industry 4.0 [4,5]. Among AM techniques, those using photocurable resins are expanding their application field. In particular, stereolithography (SLA) consists on the photopolymerization of a liquid precursor using a light source (normally in the UV range) which solidifies with a resolution in the order of microns [6,7]. Although there are some epoxy-based resin precursors, most widespread SLA precursors are of an acrylic nature [8]. In order to extend the application field of AM technologies and, in particular, of SLA, remarkable effort is carried out nowadays for the development of novel advanced materials with additional functionalities, where the development of nanocomposites is an effective strategy [9–12]. The optimization of the performance of these novel materials requires understanding the structural features obtained under different fabrication routes. In particular, characteristics such as the 3D distribution of the nano-additives within the polymeric matrix play an essential role in their potential functionality.

Electron Tomography (ET) [13] is currently a standard technique to obtain quantitative information of 3D structural and morphological features of materials at nanometric [14,15] and even atomic resolution [16,17]. This approach is based on the acquisition of a series of 2D projection images collected at different tilt angles over an angular range as large as possible to maximize resolution in 3D. After this, the reconstruction of the volume should be carried out, where a variety of algorithms have been implemented in different softwares with this purpose [18–20]. Tomography series can be obtained either in bright-field (BF)

* Corresponding author.
E-mail address: miriam.herrera@uca.es (M. Herrera).

https://doi.org/10.1016/j.polymertesting.2023.108232
Received 1 August 2023; Received in revised form 11 September 2023; Accepted 28 September 2023
Available online 30 September 2023

transmission electron microscopy (TEM) or in scanning (S) TEM mode. However, BF-TEM images of crystalline materials contain a significant contribution of Bragg scattered electrons, and such diffraction contrast images do not fulfil the projection requirement for ET, affecting the reliability of the reconstructions [21]. Since Midgley et al. demonstrated the potential of high angle annular dark field (HAADF-) STEM tomography [13,21], a broad variety of 3D structural and compositional information at the nanoscale has been obtained with this technique [15,17,22–24].

Although ET techniques have been continuously improved in the last decades, they are still limited for beam-sensitive materials such as polymers. ET requires a long time for the tilt series acquisition, therefore the specimen suffers long exposures to a relatively intense electron beam, and this may cause undesired changes within the material. Several damage mechanisms have been described for different materials, which are reviewed elsewhere [25]. In order to reduce the total electron dose (defined as the number of incident electrons per unit area that impinges on the specimen), various undersampling approaches have been proposed, which include lowering the number of 2D projection images or reducing the electron dose per image. It has recently been shown that, for a fixed total electron dose, using lower beam currents or lower dwell times (faster scanning) produce better quality reconstruction than tilt undersampling or scanning fewer pixels per image [26]. Other authors also report that large tilt increments at low electron doses yields enhanced reconstructions regarding reduced tilt increments at higher doses [27]. This evidences that the correct design of ET experiments is essential to obtain reliable results in the analysis of beam sensitive materials, as the polymeric matrices used in AM.

In order to design (S)TEM experiments in beam sensitive materials, calculation of parameters such as the critical electron dose is of great help. The critical electron dose is defined as the maximum amount of electron radiation that a sample can withstand before it suffers from radiation damage, normally quantified as the accumulated electron dose at which the monitored signal (diffraction spots, electron energy loss spectroscopy (EELS) or energy-dispersive X-ray spectroscopy (EDX) signals) decreases to 1/e (~37%) due to damage. According to Egerton [28], the critical dose for most beam sensitive materials is so low that the image resolution is no longer determined by the characteristics of the microscope and it becomes governed by the electron dose used for imaging (due to low signal to noise ratio). Regarding polymers, numerous studies have addressed the calculation of their critical electron doses by EELS and other techniques [29–32]. However, care should be taken with these values as they may only be representative for the specific conditions and microscope parameters used for their acquisition.

Specimen preparation to electron-transparency is another challenge regarding the (S)TEM analyses of polymeric materials. Preparation techniques should be able to provide clean and thin material specimens from the target material in a repeatable fashion. Common (S)TEM specimen preparation methodologies include sequential mechanical polishing and ion milling (suitable for brittle and hard materials such as ceramics and metals [33]) and ultramicrotomy, consisting on directly slicing electron-transparent sections of the material [34] and suitable for polymeric materials [35]. The use of the focused ion beam (FIB) instrument constitutes an alternative specimen preparation technique, consisting on nano-mechanization of the material using focalized Ga^+ ion beams [36]. Advantages of the FIB method includes that specimens with tailored geometry can be obtained. For electron tomography, needle-shape specimens are of interest as they allow full tilt range experiments, avoiding the undesired missing-wage effect, and also because they provide a constant thickness of the specimen during the tilting series. The FIB operation conditions need to be optimized considering the particular characteristics of each material and experiment in order to avoid damaging the material of interest [37,38].

In this work, we demonstrate that low dose ET experiments of AM polymers is feasible, and that they constitute an impulse for the development of AM nanocomposites with advanced functional properties. In particular, this work relates to SLA acrylic resins, containing either Ag nanoparticles (NPs) or WS_2 nanosheets as nano-additives, with the aim to add electrical and optical properties to the base matrix. Initially, FIB nanoneedles of this resin have been successfully fabricated. Then, a phenomenological study is carried out regarding electron beam damage in the resin. For this, attention is paid to the different parameters involved in the optimal design of low dose ET experiments in these materials. The relevance of the dose rate and of inaccuracies in the calculation of the critical dose for the design of ET experiments are discussed, in relation to previous results by the authors.

2. Materials and methods

Clear photopolymer standard resin (a mixture of proprietary acrylic monomers and oligomers and phenylbis (2,4,6-trimethyl benzoyl)-phosphine oxide as a photoinitiator) was purchased from XYZprinting, Inc (XYZprinting, New Taipei City, Taiwan). WS_2 powder was purchased from Sigma-Aldrich and silver perchlorate ($AgClO_4$) was purchased from Alfa Aesar. All products were used as received.

Two nanocomposites based in acrylic resins were fabricated. The first one was prepared using 3 wt% $AgClO_4$ precursor, and the second one with 0.4 wt% WS_2. For this, an Ultrasonic Cleaner USC500T provided by VWR (VWR International, Radnor, PA, USA) and working at 45 kHz was used for the sonication processes, 30 min in the case of $AgClO_4$. For WS_2, the powder was sonicated for 6 h, and the resultant dispersion was centrifuged (30 min) and the supernatant was decanted and mixed with the acrylic resin. Solid specimens of the nanocomposites were printed by SLA with Nobel 1.0, XYZprinting, Inc. (XYZprinting, New Taipei City, Taiwan), using a 405 nm laser with an output power of 100 mW and a spot size that allowed an XY resolution of 300 μm. All samples were printed with a layer height of 300 μm. Once printed, the samples were washed with isopropanol for several minutes. Post-processing of the samples was performed inside a UV chamber with a light source of 405 nm and a power of 1.25 mW/cm^2 (FormCure, Formlabs, Somerville, MA, USA) for 60 min.

Electron-transparent specimens for (S)TEM analyses were prepared by FIB using a Scios 2 DualBeam (Thermo Scientific) combined with FIB-scanning electron microscope (FIB-SEM). High angle annular dark field (HAADF-)STEM and Energy-dispersive X-ray (EDX) measurements were performed using a Thermo Scientific TALOS F200S (Thermo Fisher Scientific, Waltham, MA, USA) working at 200 kV. Electron doses were measured by the dose metre on the flu cam. For the electron tomography analyses, the tilt series were accurately aligned using the Inspect 3D software of Thermo Fisher Scientific Company with the cross-correlation method. The 3D reconstruction was carried out using the *simultaneous iterative reconstruction technique* (SIRT) and was visualized with the software AVIZO for FEI systems (Materials Science) 9.9.1. Simulations on interaction of Ga^+ ions with soft matter were carried out using the SRIM (Stopping Range of Ions in Matter) software [39].

3. Results and discussion

3.1. Needle-shape specimen preparation by FIB

As mentioned above, specimen preparation in the form of nanoneedles provides an excellent means to carry out ET as it prevents the progressive increase in specimen thickness during tilting usual in flat lamellae. Additionally, and of special interest for this work, this geometry facilitates the analysis of the quality of the specimen surface, to shed light at the effects of electron/ion irradiation of the material during FIB specimen preparation/STEM analyses, essential in soft materials. In this work, we have initially optimized the fabrication parameters by FIB of SLA acrylic resins for their subsequent analysis by ET.

FIB specimen preparation in the form of nanoneedles is becoming a common practice, either for its use in transmission electron tomography [40,41] or for atom probe tomography [42,43] where a specimen with

this shape is required. Details on the basic procedure used by the authors for materials such as semiconductors can be found elsewhere [44]. For polymers, the procedure needs to be optimized according to the characteristics of the material. Initially, and in order to avoid electrostatic charging during the process due to the insulating character of the resin, it is required to use some conductive material sputtering, such as Au. The basic methodology to obtain the nanoneedles starts with the extraction of a parallelepiped (around 2x8x8 μm^3) from the bulk material (similarly to the process of fabrication of electron-transparent lamellae for TEM), and for this a protective Pt layer is initially deposited on the surface of the material. Although the ion beam is normally used to obtain this Pt layer, for sensitive materials such as polymers a Pt layer needs to be deposited first with the electron beam, to reduce damage. After this, a piece of material with size of approximately 2x2x8 μm^3 is glued to a grid with a micromanipulator. In order to mill a needle from this parallelepiped, an annular pattern is used, where the inner and outer diameters are progressively reduced. The selection of currents and voltages in this process is key to obtain good quality, reduced diameter needles, as it will be explained below.

The Ga^+ ion beam used for milling the specimen to the desired shape may damage the material surface through amorphization, beam heating or ion implantation, among others. Amorphization is a main issue in crystalline materials, as reported previously by the authors [44]. In polymers, beam heating due to FIB preparation has been reported to be limited by maintaining low beam currents (<100 pA) during milling [38]. In general, ion implantation acquires remarkable importance in soft materials such as polymers. Ion implantation depends on the characteristics of the material, on the ion/electrons voltage used for milling and on the incidence angle between the ion beam and the specimen surface. In needle-shape specimen preparation, the ion beam is almost parallel to the specimen surface, which should reduce implantation rates in comparison to a perpendicular incidence (as it will be shown below). Optimizing the working parameters of the FIB for specimen preparation is essential to reduce/avoid material damage due to the ion beam incidence. In order to shed light on possible Ga^+ ions implantation in the material during milling, simulations of the interaction of the Ga^+ ions beam and the polymer surface have been carried out. In particular, the effect of the ion acceleration voltage has been analysed. For this, the incidence angle between the ion beam and a vector normal to the specimen surface has been considered as 89° and a material with an expected behaviour similar to the acrylic resin (epoxy resin) has been selected from the available database. Fig. 1a) shows the results of the simulation for a voltage of 30 kV. As it can be observed, on average the penetration depth of the Ga^+ ions in the resin is of 5.2 ± 3.4 nm. A reduction of the acceleration voltage may reduce this penetration depth. Simulations for voltage values of 16, 8, 5 and 2 kV have also been computed, and the results are included in Fig. 1b). As it can be observed, the penetration depth is progressively reduced with voltage to values as low as 1.4 ± 0.9 nm for a voltage of 2 kV. This suggests that the damage to the specimen surface during specimen preparation is reduced with lower voltages. However, this extremely low voltage is not appropriate for needle-shape specimen preparation because the quality of the images obtained is very low which complicates the procedure, and also because the milling time is too long, therefore it can only be used for final cleaning steps. A design of the needles fabrication process for acrylic resins has been carried out considering a balance between the process duration time and the reduction of the needle surface damage. This process is detailed in Fig. 1c), where the initial stage consists of a piece of material with size of approximately 2 × 2 μm^2 glued on a TEM grid as explained above. As it can be observed in Fig. 1c), the inner/outer

a)

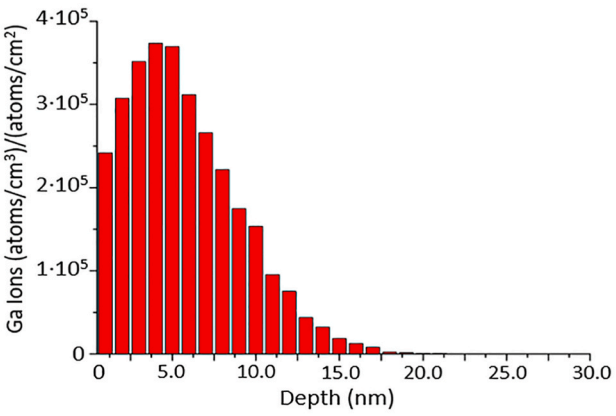

b)

Ion Voltage (kV)	Ion Range (nm)
30	5.2 ± 3.4
16	3.6 ± 2.3
8	2.6 ± 1.7
5	2.0 ± 1.3
2	1.4 ± 0.9

c)

	First milling step	Second milling step	Third milling step
Electron current (pA)	30	25	12
Voltage (kV)	30	8	8
Outside diameter (nm)	1800	1100	600
Inside diameter (nm)	900	500	150
Depth of milling (nm)	500	500	500

d)

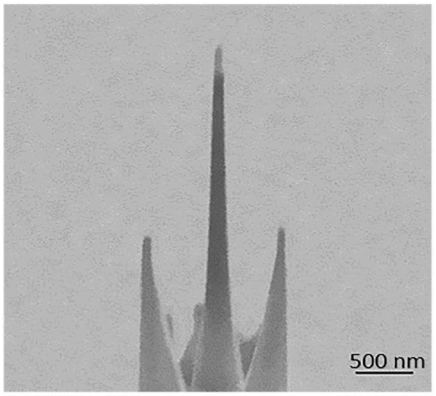

Fig. 1. a) Simulation of Ga^+ ions penetration depth for 30 kV and parallel incidence; b) Results of the simulation of Ga^+ ions penetration depth for varying ion voltages; c) Summary of the optimized steps for the fabrication of needle-shape specimens of SLA acrylic resin; d) SEM image of a needle-shape specimen of acrylic resin fabricated by FIB following the procedure in c).

diameter of the annular pattern is progressively reduced in three steps. In order to avoid protuberances, it is important that the outer diameter in each step is larger than the inner diameter of the previous step. These milling steps are followed by cleaning steps at low voltage. In the last cleaning step, a rectangular pattern instead of the annular one can be used, milling for as long as the Pt layer can withstand. With these parameters, needles with diameters below 100 nm as that shown in Fig. 1d) can be obtained, ideal for ET analyses.

In order to obtain experimental evidences of the surface quality of needle-shape specimens fabricated by FIB using different voltages for the final cleaning steps, EDX analyses have been carried out. Fig. 2a) shows a HAADF-STEM image of a specimen obtained at 30 kV, where some bright spots can be observed on the surface of the needle. In HAADF-STEM, the intensity is proportional to the average atomic number (Z) of the material. This evidences that the surface of the polymeric specimen, which is mainly composed of the low Z number atoms C and H ($Z_C = 12$, $Z_H = 1$), is contaminated by larger Z atoms, presumably Ga ($Z_{Ga} = 31$). In order to evaluate this, EDX analyses have been carried out, shown in Fig. S1. As it can be observed, this analysis has evidenced the presence of Ga on the surface of the needle-shape specimen, due to the milling process.

Needle-shape specimens obtained using lower voltages for the final steps of milling/cleaning have also been fabricated and analysed by EDX, and EDX line profiles are included in Fig. 2b). As it can be observed, a clear reduction in Ga^+ implantation is found when reducing the ion beam voltage from 30 kV to 8 kV. This tendency is in good agreement with the results obtained in the simulations of Ga^+ penetration depth shown in Fig. 1b). However, a notable difference is found in the quantitative values of penetration depth, as they seem to be larger in the experimental measurements. Also, it is worth noting that the EDX profiles show a curved shape. These results could be due to the projection effect that takes place during TEM analyses. The inset of Fig. 2c) shows a schematic of two concentric cylinders, with radius of 50 nm and 44.8 nm respectively, modelling a (Ga) shell of 5.2 nm (according to the SRIM simulations) on the surface of a needle-shape specimen. Fig. 2c) shows a linescan of the shell thickness of this model when projected on a plane parallel to the cylinder axis. As it can be observed, the shape is similar to that obtained in the EDX linescan, evidencing that Ga is preferentially located on the surface of the nanoneedles, as expected. On the other hand, it is worth noting the asymmetry observed in the experimental EDX linescans, more noticeable for larger voltage. In soft materials such as polymers, slender needles (when the dimensions of its cross-section are small compared to its length) sometimes are not stable enough to stay vertical during the milling procedure, and they suffer from what is known as *buckling*, as shown in Fig. 2d). This produces an increase of the angle between the incidence ion beam and the specimen surface in one side of the needle. Fig. S1b) shows a simulation of the interaction between the ion beam and the specimen surface for different incidence angles, evidencing an increased interaction depth for larger ion beam incidence angles. Thus, bending of needle-shape specimens during the preparation process leads to a progressive increase in Ga^+ implantation and then, in surface damage. Although this buckling has shown to be random to some extent according to a number of experiments carried out by the authors, it is of

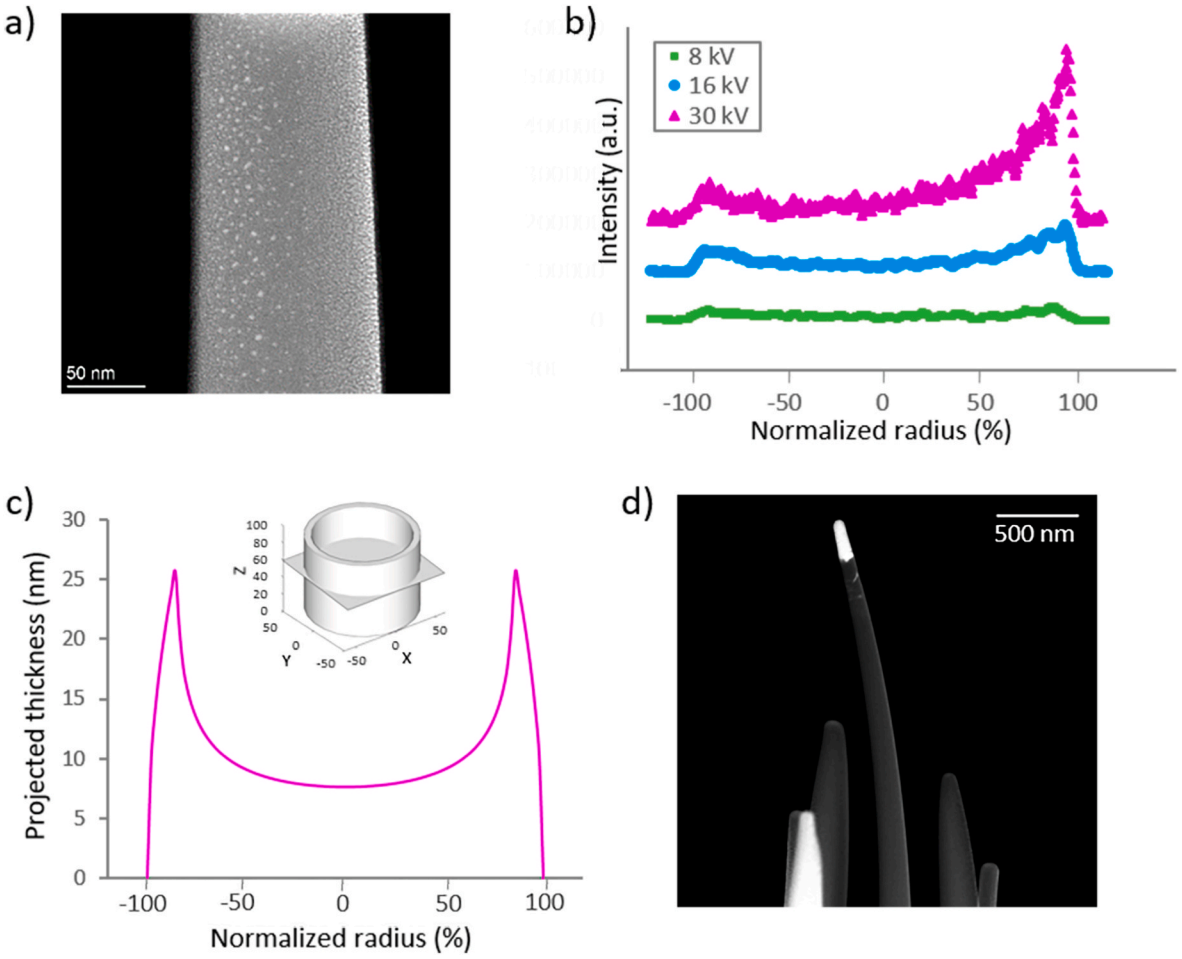

Fig. 2. HAADF-STEM image of a needle-shape specimen of acrylic resin fabricated at 30 kV by FIB; b) Ga EDX line profiles of needle-shape specimens obtained using decreasing voltages for the final steps of milling/cleaning; c) linescan of the shell thickness projected on a plane parallel to the cylinder axis obtained from the model in the inset; d) HAADF-STEM image of a needle that became bent during the fabrication process.

interest to reduce the length of the fabricated needles to increase their stability and reduce the surface damage caused by the ion beam of the FIB.

3.2. Low dose ET conditions

Regarding the ET analyses of the SLA nanocomposite needle-shape specimens fabricated by FIB, as explained above these analyses require the acquisition of series of images obtained at increasing tilting angles, and because of this the electron dose applied to the material is larger than in conventional 2D analyses. Nowadays, large efforts are paid to reduce the electron dose used in ET both in TEM and STEM [27, 45–49], sometimes using advanced instrumentation such as the direct electron detector [50] or the monochromator [51]. This is essential for polymer materials, with critical doses that are usually low [31]. In particular, for the acrylic resin considered in the present study, previous results by the authors obtained by core loss EELS showed that the decrease in oxygen/carbon signals reached their critical values (i.e., falling of the initial oxygen reference by a factor e) at accumulated doses lower than 10^2 e/Å^2/~$7{\cdot}10^2$ e/Å^2, respectively [52]. It was also reported a critical dose on the order of 10^3 e/Å^2 for a reduction of thickness during irradiation measured by low loss EELS [52]. However, calculated critical electron doses depend on the specific microscopy settings used such as voltage [53], temperature [54] or dose rate [29]. Those analyses by the authors were carried out in an aberration corrected microscope (FEI Titan Themis). In the present work and based on those previous results, we carry out a phenomenological analysis of the optimum conditions to perform HAADF-STEM tomography in needle-shape specimens of SLA nanocomposite materials, this case in a non-aberration corrected microscope (FEI Talos F200S).

The acquisition of tomography series requires of a careful design of the microscopy settings, where the electron dose applied to the material is inferior to its specific critical electron dose. The calculated electron doses should include both the dose applied for the acquisition of the images and the dose used for locating the region of interest, focusing, etc. It is also necessary the appropriate design of the parameters related to the ET series, which are the tilt range and the tilt increment.

In STEM, the electron dose applied to the material depends on the electron current of the probe, on the dwell time of the probe in each pixel and on the pixel size of the image. In order to control the electron dose during STEM analyses, those parameters need to be careful chosen. The electron current in STEM is controlled by the spot size and by the gun lens (and, for microscopes with the specific instrumentation, by the monochromator). For a specific value of the gun lens, modifications of the spot size in the microscope FEI Talos have a strong effect on the electron current, as it can lead to currents that ranges between 1 nA and <0.03 nA. However, the spot size has also a strong effect on the spatial resolution, therefore when analytical measurements are not required small spot sizes are usually utilized. For a fixed spot size, modification of the gun lens in a reasonable interval has a lower effect in the electron current, which can be varied at most in 0.1 nA. The condenser lens aperture would also affect the electron current, but normally in a non-aberration corrected microscope the smallest aperture is required to prevent the aberrated beams from participating in the image formation. Regarding the dwell time, a balance should be found in the selection of this parameter. Short dwell times reduce the signal/noise ratio therefore worsening the quality of the image. However, too long dwell times increases the acquisition time of each image, may introduce artefacts if image drift occurs due to poor stability, and produces larger hydrocarbon contamination, typical in organic specimens. Dwell times in STEM are usually in the range 1–20 μs, therefore in order to minimize the drawbacks explained above we use intermediate values of 10 μs. It has been reported that a low dwell time of 0.5 μs during STEM imaging in a microscope JEOL JEM-2100F produces a streaking artefact parallel to the scan direction, likely due to a slow reaction time of the photomultiplier or read-out electronics leading to an anisotropic smearing out of individual signal peaks, which is noticeably reduced when increasing the dwell time to 2 μs [55]. Finally, and regarding the pixel size where the electron current is applied, it depends both on the image magnification and on the image resolution. The image magnification is normally determined by the features that need to be studied, and because of this it can only be slightly modified. In the present work, a magnification of 450 kx is appropriate for the analysis of the distribution of WS_2 sheets or of Ag NPs in the acrylic resin, as it will be shown later. The image resolution affects the quality of the information acquired, and influences the acquisition time of each image. The image resolution ranges from 128 × 128 to 4096 × 4096, although for imaging low resolution values (smaller than 512 × 512) should be avoided. Images acquired at a resolution of 2048 × 2048 require 4 times more time than an image acquired at 1024 × 1024 (in electron tomography, this excess time needs to be multiplied by the number of images, normally in the range 70–140), and usually the hydrocarbon contamination is worse. Our experiments have shown that image resolution of 1024 × 1024 is reasonable for our analyses.

Table 1 shows calculated electron doses for different STEM image acquisition parameters, for dwell time of 10 μs. As it can be observed, electron doses range between 1 and 10^7 e/Å^2 depending on selected microscope settings, therefore the analysis conditions need to be carefully selected for beam sensitive materials. The modification of different acquisition parameters has different effects on the electron dose. For example, doubling the electron current or the dwell time implies doubling the electron dose, whereas changing from image resolution of 1024 × 1024 to 2048 × 2048, the electron dose is multiplied by 4. On the other hand, increasing either dwell time or image resolution increases acquisition time, whereas increasing electron current does not. In order to understand the effect of the electron beam on a specific material, it is useful fixing a reasonable magnification and image resolution (that would depend on the features to be analysed), and modifying the electron current to obtain the desired electron dose.

With the aim to obtain information on the behaviour of specimens of acrylic resin during analyses by HAADF-STEM ET carried out using different electron doses, we have designed different experiments where 70 images are sequentially acquired, simulating a tomography experiment with a tilt range of ±70 and a tilt increment of 2°. For these experiments, needle-shape specimens are ideal as they allow easily keeping track on the specimen thickness, which may have a special influence on the integrity of the material. Needles with thickness close to 100 nm have been considered for this experiment, as this thickness constitute a reasonable compromise value: on the one side, thicker specimens are desirable in these ET analyses in order to sample a larger number of features of interest inside the material; on the other side, the material needs to be electron-transparent. Regarding the imaging conditions, as stated above for the specific additives considered in this work magnifications of 450 kx are reasonable values; also, images obtained at a resolution 1024 × 1024 with dwell time of 10 μs are considered, and only the electron current is modified to change the electron dose. The electron doses considered are in the range 10^2-10^4 e/Å^2 for individual images, as critical electron doses calculated previously using EELS experiments are on the order of 10^3 e/Å^2, as it will be discussed later [52].

Fig. 3a) shows an image of a needle-shape specimen of acrylic resin sculpted by FIB. Before obtaining this image, initially the magnification was set at 450 kx (at screen current of 0.55 nA), and positioning of the nanoneedle and focusing was carried out, taking as few as 5 s. However, and as it can be observed, during the focusing process (and before any image was acquired) the needle already suffered noticeable damage, as the accumulated dose during this focusing process reached $4{\cdot}10^3$ e/Å^2. This shows that care should be taken during positioning and focusing of the material under the electron beam, because even when fast scan is used, the accumulated dose could be too large for the material to withstand it. As shown in the inset of Fig. 3a), a dark region has appeared in the central part of the needle upon electron irradiation. In HAADF-STEM images, the intensity scales with Z^n (Z = atomic number),

Table 1
Electron doses (e/Å^2) in STEM mode for different settings of the FEI Talos F200S, for dwell time of 10 μs.

Magn.	512 × 512			1024 × 1024			2048 × 2048			4096 × 4096		
	Current (nA)											
	0.01	0.3	1	0.01	0.3	1	0.01	0.3	1	0.01	0.3	1
160kx	6.3	$1.9{\cdot}10^2$	$6.3{\cdot}10^2$	$2.5{\cdot}10^1$	$7.6{\cdot}10^2$	$2.5{\cdot}10^3$	$1.0{\cdot}10^2$	$3.0{\cdot}10^3$	$1.0{\cdot}10^4$	$4.1{\cdot}10^2$	$1.2{\cdot}10^4$	$4.1{\cdot}10^4$
450kx	$5.1{\cdot}10^1$	$1.5{\cdot}10^3$	$5.1{\cdot}10^3$	$2.0{\cdot}10^2$	$6.1{\cdot}10^3$	$2.0{\cdot}10^4$	$8.1{\cdot}10^2$	$2.4{\cdot}10^4$	$8.1{\cdot}10^4$	$3.2{\cdot}10^3$	$9.7{\cdot}10^4$	$3.2{\cdot}10^5$
1.3Mx	$4.0{\cdot}10^2$	$1.2{\cdot}10^4$	$4.0{\cdot}10^4$	$1.6{\cdot}10^3$	$4.9{\cdot}10^4$	$1.6{\cdot}10^5$	$6.5{\cdot}10^3$	$1.9{\cdot}10^5$	$6.5{\cdot}10^5$	$2.6{\cdot}10^4$	$7.8{\cdot}10^5$	$2.6{\cdot}10^6$
2.55Mx	$1.6{\cdot}10^3$	$4.9{\cdot}10^4$	$1.6{\cdot}10^5$	$6.5{\cdot}10^3$	$1.9{\cdot}10^5$	$6.5{\cdot}10^5$	$2.6{\cdot}10^4$	$7.8{\cdot}10^5$	$2.6{\cdot}10^6$	$1.0{\cdot}10^5$	$3.1{\cdot}10^6$	$1.0{\cdot}10^7$

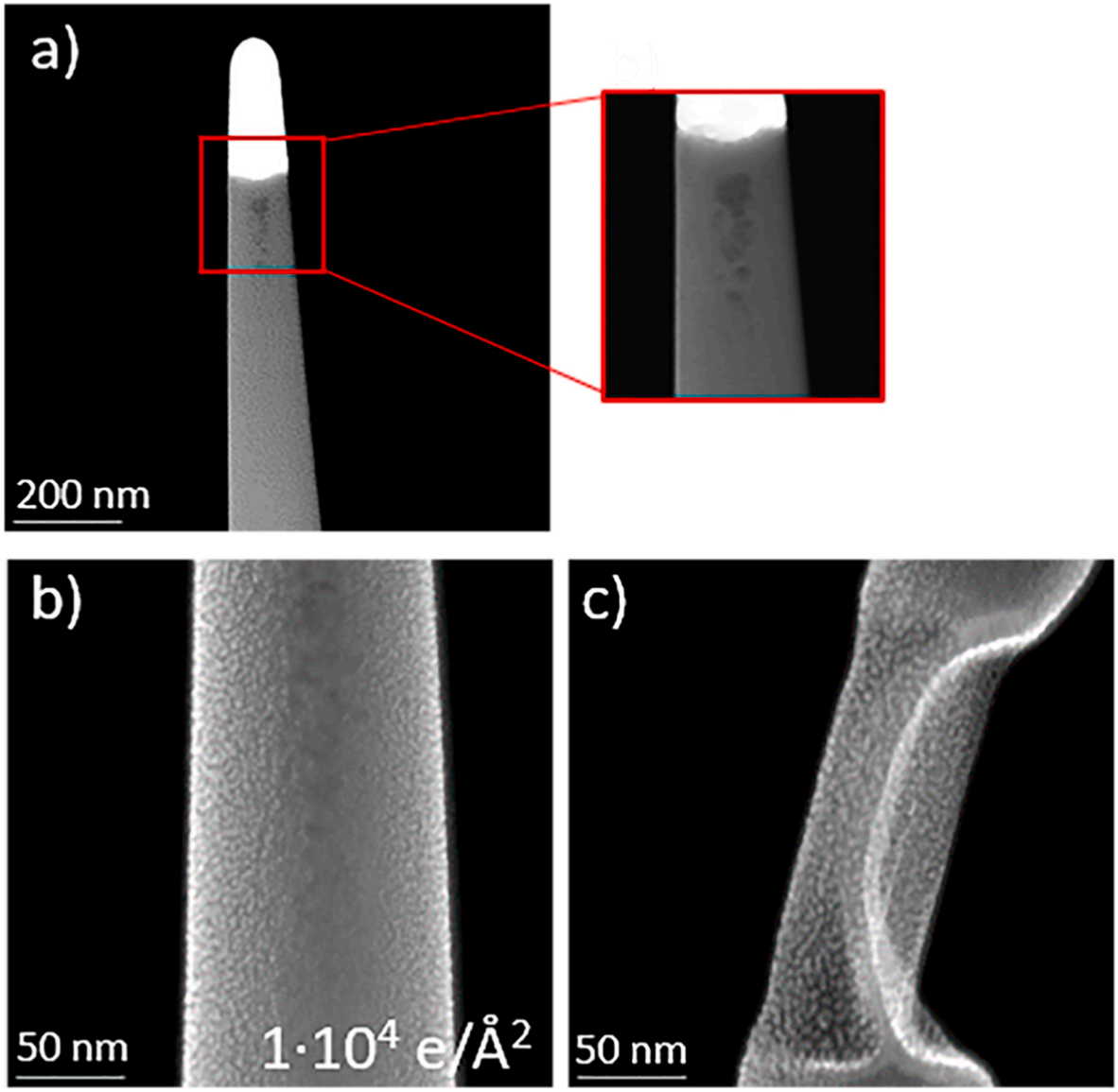

Fig. 3. a) HAADF-STEM image of a needle-shape specimen of acrylic resin sculpted by FIB, where a dark region due to electron beam damage during focusing can be observed (amplified in the inset); b) and c) 1st and 70th images of a HAADF-STEM images series obtained at electron dose of $1{\cdot}10^4$ e/Å^2.

and for the same Z, the intensity increases for larger thicknesses. According to this, the dark region observed in Fig. 3a) indicates regions of smaller amounts of material or cavities inside the needle, produced because of damage due to the electron beam. In our previous work and according to STEM-EELS results, it was proposed that damage to this acrylic resin under the electron beam occurred initially through a process of radiolysis followed by knock-on phenomena until breakage [52]. Radiolysis is a common damage mechanism for organic materials [25,56–58]; however, in some studies radiolysis and knock-on damage taking place sequentially have also been reported [56,59], as knock-on damage normally requires larger accumulated doses. Detailed analysis of the spectral shape and evolution of core-loss EELS fine structure pointed to two possible scission pathways of the acrylic resin. The first one considers the breakage of the carboxylic C–O bond, resulting in the formation of RO· and acyl radicals leading to the emission of CO molecules; the second one involves the removal of the carboxylic radical, and the by-side formation of carbon radicals, with the emission of CO and CO_2. Other studies also pointed to the degradation of carboxylic

groups and the formation of different radicals and the emission of small molecules as the starting point of resin degradation [60,61]. These degradation mechanisms justify the formation of small cavities inside the needles upon electron exposure, what explains the dark contrasts observed in the HAADF-STEM images as the result of damage in the material. In the following experiments, focusing has been carried out at the bottom of the nanoneedles, out of the region of interest, and at lower magnification, to avoid damaging the material previously to the image acquisition.

An experiment of obtaining a 70 images series with an electron dose of $1{\cdot}10^4$ e/Å^2 per individual image has been carried out, and the 1st and 70th images are shown in Fig. 3b) and c), respectively. As it can be observed, a fine dark speckle is observed at the central part of the needle from the initial image obtained, more evident in the thinner part of the needle. On increasing the electron dose, a reduction in the needle diameter occurs (see some of the intermediate images of this series in SI, Fig. S2a) to f)), that becomes irregular for larger exposure times, and that leads to a final bending of the needle. The elimination of small molecules caused by the radiolysis process due to the impinging electrons may form cavities inside the needle, causing structural failure. As expected, this electron dose is excessive for the tomography analysis of this material.

Results of images series acquired at slightly reduced electron doses ($8{\cdot}10^3$ e/Å^2 for each individual image) are shown in Fig. 4a) to c) (additional images of this series are included in Supporting Information, Fig. S3a) to f)). As it can be observed, damage in the thinner region of the needle (diameter of 90 nm) is noticeable earlier than in the thicker part (diameter of 105 nm). It has previously been reported that radiation sensitivity for certain materials may depend on the initial thickness of the specimen [62]. Also, previous results by the authors showed that critical doses of acrylic resins under EELS conditions reached values five times larger for specimens with thickness above 50 nm regarding those of thickness below this value [52]. These results show the importance of specimen thickness in the material integrity during (S)TEM and, especially, during ET analyses. Here, from around the 10th image (see SI Fig. S3a)), some fine speckle is already noticeable in the thinner region of the needle. It should be noted that some damage is likely to occur before it is noticeable in the HAADF images, therefore care should be

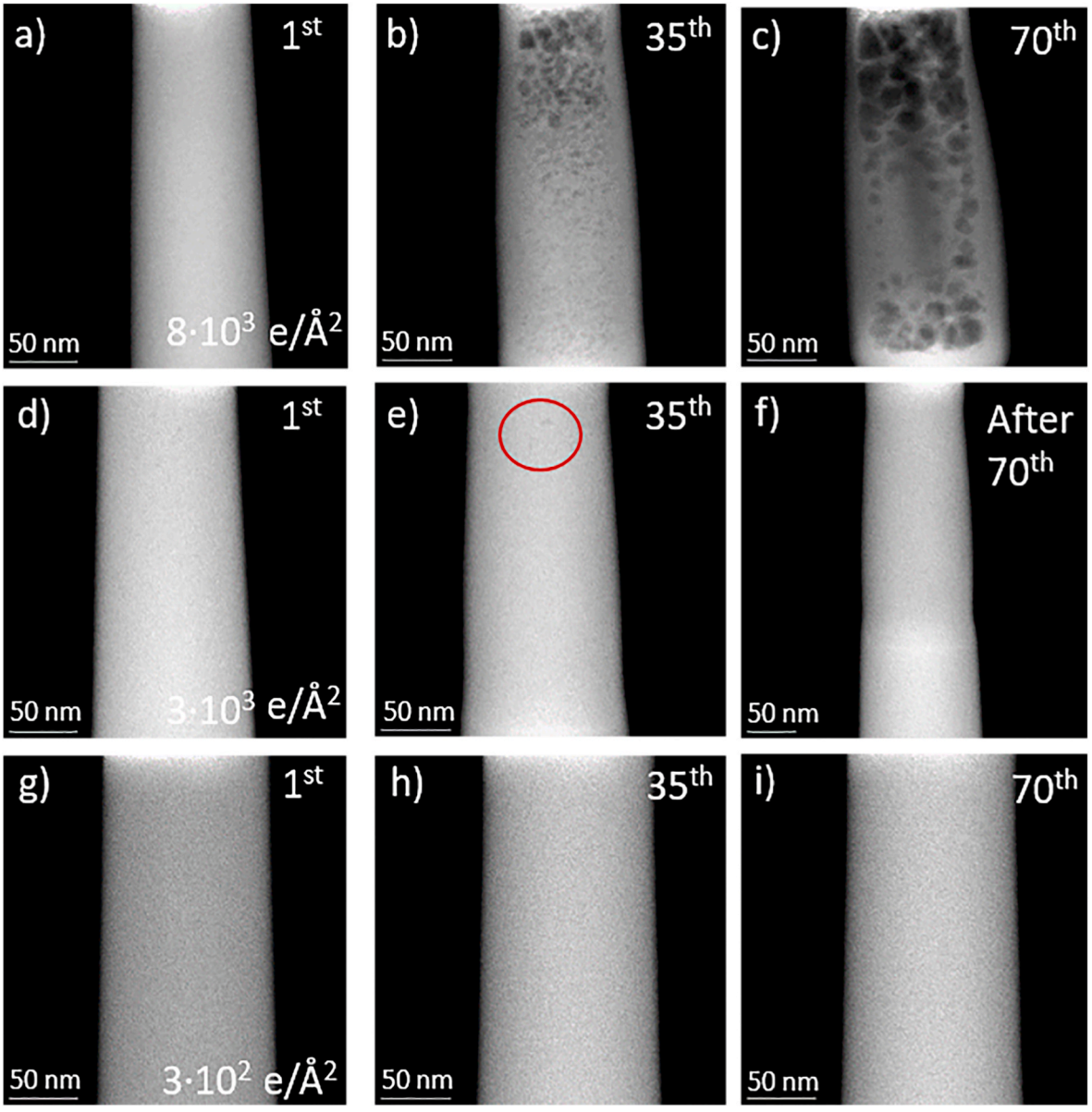

Fig. 4. 1st, 35th and 70th images of HAADF-STEM image series obtained at electron doses of $8{\cdot}10^3$ e/Å^2 (a) to c)), $3{\cdot}10^3$ e/Å^3 (d) to f), where f) shows an image obtained after the 70th and at lower magnification to better reveal the reduction in diameter), and $3{\cdot}10^2$ e/Å^2 (g) to i)).

taken when working with electron doses that are too close to those where damage is already visible. Increasing the accumulated dose, elimination of material progresses, being evident also in the thicker regions of the needle, and catastrophic failure is observed. The same results have been observed in a second experiment carried out at a similar electron dose, of $6{\cdot}10^3$ e/Å^2, and shown in Fig S4a) and b).

However, on reducing the electron dose to $3{\cdot}10^3$ e/Å^2, a different behaviour has been observed. Fig. 4d) to f) show images of a series acquired from a needle with average diameter of 108 nm. As it can be observed, only a faint speckle is found in the central part of the needle (see Fig S3g) to l) for additional images of this series) and most noticeably, a reduction in the needle diameter is clearly observed when increasing the accumulated electron dose. Results of an additional experiment with similar electron dose ($2{\cdot}10^3$ e/Å^2) and the same observations can be found in SI (Fig S4c) and d)). The observed diameter reduction seems to be the result of surface erosion at the edges of the needle due to the electron beam, although the formation of small cavities inside the material upon electron exposure may also have some effect. The edge of the needle has a much smaller thickness than its central part and, as shown above, the thickness of the material has an important effect on the damage process. Thus, it may be this weakness of the edge of the needle because of its lower thickness what produces a more focused damage in this region, and this damage mechanism seems to occur more noticeably than voids formation at these lower electron doses.

Finally, an images series has been acquired at lower values of electron doses, $3{\cdot}10^2$ e/Å^2 for each individual image. As it can be observed in Fig. 4g) to i) (additional images are found in Fig S3m) to q)) no evident damage is observed through the 70 images acquisition, despite the relatively large accumulated dose at the end of the experiments, of $2{\cdot}10^4$ e/Å^2. The same result has been obtained for an additional images series acquired at $4{\cdot}10^2$ e/Å^2 and shown in Fig S4e) to f).

Our experiments have shown that acquisition of individual HAADF-STEM images at electron doses of 10^4 e/Å^2 produce serious damage to the resin needle-shape specimens, whereas acquisition of series of 70 images with accumulated doses of 10^4 e/Å^2 does not. This suggests that the dose rate (defined as the number of incident electrons per unit area per unit time impinging on the specimen) may have a strong influence on the effect of the electron beam in the material. Dose rate dependent electron damage has been reported for a variety of materials, including ionic materials [63] and organic materials [64]. A direct dose-rate effect is attributed to materials with larger radiation sensitivity for elevated dose rate, which sometimes is associated to the poor electrical conductivity and accumulated charging [25]. On the other hand, an inverse dose-rate effect is related to decreased radiation sensitivity for increased dose rate, and this could originate from slower beam damage events such as diffusion-limited mass loss, precipitation and segregation [25]. In ET, care should be taken in the evaluation of the electron dose rate used, because of the singularity of the experiments. Dose rates (as well as electron doses) in STEM are typically calculated per pixel of an image. Thus, in the acquisition of individual images at doses of 10^4 e/Å^2 in our work, the electron dose rate per pixel used is of 10^9 e/Å^{2}s. However, in the acquisition of series of 70 images with accumulated doses of 10^4 e/Å^2 the calculation of the dose rate is not so straightforward. Although the dose rate per pixel in each image in this case is of 10^7 e/Å^{2}s, the accumulated dose of 10^4 e/Å^2 is only obtained after the acquisition of 70 images. In this case, individual images are obtained with an interval of around 2 s between each other, therefore the full series is acquired in more than 800 s. Because of this, the dose rate is highly non-uniform in time, and the average dose rate is much smaller than that calculated above, showing remarkable differences between the two experiments in the manner the dose is applied. In any case, it seems that the lower dose rate utilized in the second case could be responsible for the reduced damage. Thus, our results show that when accumulated doses of 10^4 e/Å^2 are applied at very low dose rates in acrylic resins, no evident damage is observed by HAADF-STEM, in contrast to large dose rates. These results suggest that, for the microscope characteristics and operation conditions used, and for the nature and thickness of the material under study, the critical electron dose is lower than $3{\cdot}10^2$ e/Å^2, which is the electron dose used for individual images. In this case, if either no damage occurs during every single irradiation event or if only reversible phenomena takes place, the sum of isolated irradiation events does not have a deleterious effect in the material. Critical doses in the range 10^3-10^5 e/Å^2, similar to the electron dose used in our experiment, have been reported for different polymers in the non-aberration corrected microscope [25,29,31,65–67], although as it will be discussed below care should be taken in the direct comparison of (critical) electron dose values calculated for different microscopy settings.

Regarding our previous analysis of this acrylic resin by EELS in an aberration corrected microscope [52], it showed that for electron doses below 10^2 e/Å^2 (and from the starting of the irradiation process) the mass loss followed a first order process with an exponential dose dependence, which suggested the main role of radiolysis in this process. For doses above 10^2 e/Å^2, the mass loss showed to be directly related to the accumulated dose, in agreement with a zero-order process pointing to a knock-on damage mechanism for these larger doses. According to this, it seems that radiolysis should be already taking place in the images obtained at 10^2 e/Å^2 in our experiments in the non-aberration corrected microscope. However, no evident damage is observed in these images, nor it is found after the accumulation of 70 irradiation events. Again, differences in the results obtained in the aberration corrected microscope and in the non-corrected instrument are related to the different parameters used in the experiments, and could stem from different reasons. On the one hand, the specimen thickness is different in both experiments, being of about 50 nm in the first one (Titan) and of 100 nm in the present study (Talos). Thickness has shown to have an important effect in electron beam damage, as discussed above (Fig. 3a)). On the other hand and as previously pointed by other authors [68], calculated critical doses determined in different experiments may not be directly comparable due to usual simplifications in the calculations. In STEM, each dwell location suffers direct irradiation at high dose rates. When the probe size is smaller than the pixel size, the areas between these dwell locations are not irradiated; on the other hand, for probe sizes larger than the pixel size, adjacent pixels are also irradiated during the scanning. However, calculations of electron doses consider that the electron current is equally spread in the full pixel size, every pixel being irradiated only once per scan. Thus, dose calculations normally overlook parameters like probe-size and distance between dwell locations, which influence the effective doses experienced by the sample. For example, Siangchaew et al. [57] showed that the reduction in the distance between pixels from 80 nm to 5 nm when acquiring EELS digital linescans of polyethylene produced a reduction in π-peak intensity associated to increased damage, evidencing the importance of the distance between dwell locations. Regarding the probe size, although in a particular microscope in STEM mode it may vary slightly for different settings, it is generally smaller in an aberration corrected microscope regarding the non-corrected instrument. Fig S5a) and b) show images of the probe size for usual imaging conditions in the Titan microscope and in the Talos, respectively, and Fig S4c) shows linescans obtained from the images in a) and b). In the Titan microscope, the probe size in STEM in usual imaging conditions is of the order of 0.3–0.6 nm, whereas in the Talos the probe size is around 1–1.5 nm, 2–4 times larger, which affects both the effective electron dose and the dose rate of the experiments, both larger in the Titan microscope. However, in the Talos microscope the probe size is larger than the pixel size for most magnification/image resolution combinations (included those used in our experiments), therefore each pixel is irradiated more than once per image, increasing the calculated electron dose. Here, the dose rate is not uniform, as the beam can reach each pixel in successive scan lines, and the average dose rate for an equal electron dose is definitely larger in the Titan microscope. Because of these facts, a direct comparison between the conditions of electron beam exposure in both microscopes is not possible, and

phenomenological studies are of great help to understand the behaviour of a material under the electron beam for specific microscope settings and specimen characteristics. It seems that the larger dose rate used in the Titan joined to the smaller specimen thickness in our previous study should explain the larger sensitivity found in the material when analysed in the aberration corrected microscope.

3.3. ET experiments

In order to show the feasibility and the interest of carrying out ET of SLA nanocomposites, we have performed preliminary experiments in selected materials. Fig. 5a) shows a HAADF-STEM image of a nanoneedle sculpted by FIB (following the steps explained earlier), obtained from an object fabricated by SLA. The material consists of a composite composed of 0.4 wt% of WS_2 in an acrylic resin. The addition of 2D transition metal dichalcogenides to polymer nanocomposites has attracted great attention recently because of different reasons. For example, composites of MoS_2 and $MoSe_2$ have been proposed as saturable absorbers for the production of fibre lasers [69,70]; MoS_2 has also been used in polymer composites as an additive to reduce wear and improve fire retardancy [71,72]; BN and MoS_2 have been used for mechanical reinforcement of polymers [73,74]. In particular, the addition of WS_2 to SLA acrylic resins is expected to improve the mechanical properties and increase the thermal and electrical conductivity of the material, opening the use of SLA pieces for new applications [75–79]. Reaching the percolation threshold for thermal/electrical conductivity requires an efficient exfoliation of WS_2, which could take place by sonicating the 2D material directly in the liquid resin or using an intermediate solvent. In the first case the fabrication process is simpler, in the second one the exfoliation rate is higher. The parameters used for the fabrication process (sonication time, use of solvent, amount of WS_2) will determine the functional properties of the material, and they need to be optimized. For this, the analysis of the 3D structural characteristics of the WS_2 inside the acrylic resin (density, distribution, etc.) is essential to understand the functional properties of the material. In the image in Fig. 5a), the brighter regions inside the needle of acrylic resin correspond to the additive of WS_2, with larger Z number than the matrix (see also an EDX analysis in Fig. SI6a)). A tilt series over an angular range of −70/+66 has been acquired with a step of 2°, using electron doses of $5.0{\cdot}10^2$ e/Å^2 for each image, which results in a total electron dose of $3.5{\cdot}10^4$ e/Å^2. Under these conditions, the structural integrity of the nanoneedle has been preserved during the tomography series acquisition. The reconstruction of the data using the algorithm SIRT has allowed obtaining information about the WS_2 material inside the composite. As it can be observed in Fig. 5b), c) and d), where snapshots from the reconstructed data are included (see also a video in Supporting Information), layers with size up to 90 nm long have been observed. Although the resolution obtained in this analysis is not enough to quantify the number of monolayers present in the material, it can be observed that a reasonable exfoliation degree has been achieved upon sonication (before sonication, the commercial WS_2 powder used has a size of 2 μm). Additionally, the 3D spatial distribution of the layers is obtained, evidencing regions where the layers are in contact and other where they are not (pointed by arrows in Fig. 5b) and d)). The distribution of the material in the resin is of remarkable importance to shed light at the basic mechanisms for thermal/electrical conductivity in those optimized composites where the percolation threshold is reached. An analysis of the effect of using different solvents and increasing amounts of WS_2 in the structural and thermal/electrical properties of the material is in progress to optimize the development of these novel SLA conductive nanocomposites, and will be published elsewhere. In order to obtain statistical information on the WS_2 layers distribution within the matrix, electron microtomography [80–82], where thicker specimen layers can be used, is also in progress.

Although needle-shape specimens have proven useful for electron tomography of SLA nanocomposites, the amount of material analysed when working with these needles is not large, and sometimes the larger field of view that specimens in the shape of lamella can provide is useful when working with particular nano-additives. Such is the case of nanocomposites with metallic NPs incorporated as nano-additives. We are working in the development of conductive nanocomposites where Ag NPs are synthetized *in-situ* in the acrylic resin during the photopolymerization process by SLA [83], to avoid the NPs agglomeration expected for ex-situ synthetized NPs. A good distribution of small NPs throughout the material is essential to increase the electrical conductivity of the composite. As the solubility of the Ag NPs precursors in the acrylic resin has been found to be a limiting factor in the amount of NPs that can be obtained [83], the use of intermediate solvents to increase the solubility of the Ag precursor is being tested [84]. Understanding the electrical behaviour of the final composites requires a careful analysis of the Ag NPs density, size and distribution through the polymer matrix, where electron tomography experiments could play an essential role. Fig. 6a) shows a HAADF-STEM image obtained at low dose ($3.8{\cdot}10^2$ e/Å^2) of a lamella fabricated by FIB from a SLA nanocomposite with a 3 wt% $AgClO_4$. Ag NPs can be clearly observed in the polymeric matrix thanks to their larger intensity regarding the acrylic resin due to larger Z number (see also EDX analysis of Ag NPs in Fig. SI6b)). A tilting series has been acquired over a tilting range of ±60 and with a step of 2°, resulting in a total electron dose of $2.3 \cdot 10^4$ e/Å^2. Fig. 6b) and c) shows snapshots from the reconstructed data (see a video in Supporting Information), exhibiting a good distribution of Ag NPs. Fig. 6d) shows a histogram of the size distribution of the Ag NPs, where it is shown that more than 200 NPs has been found and most of them have size below 6–7 nm^3, which is very advantageous to increase the electrical conductivity. It should be mentioned that NPs with smaller sizes (not resolved in the tomogram) are likely present in the material, being the spatial resolution of the analysis carried out limited due to the low electron dose used, and also due to the large region of the material

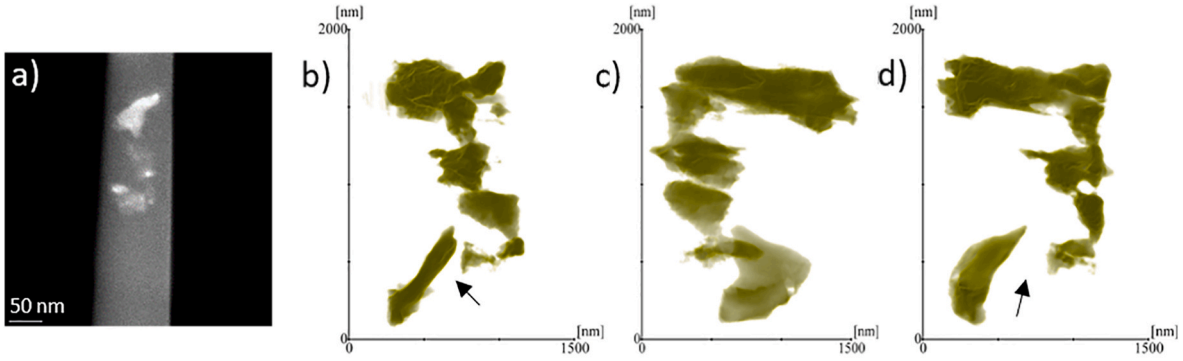

Fig. 5. a) HAADF-STEM image of a needle-shape specimen of a nanocomposite of 0.4 wt% of WS_2 in an acrylic resin; b) to d) snapshots obtained from the reconstructed data of an ET analysis of the specimen in a).

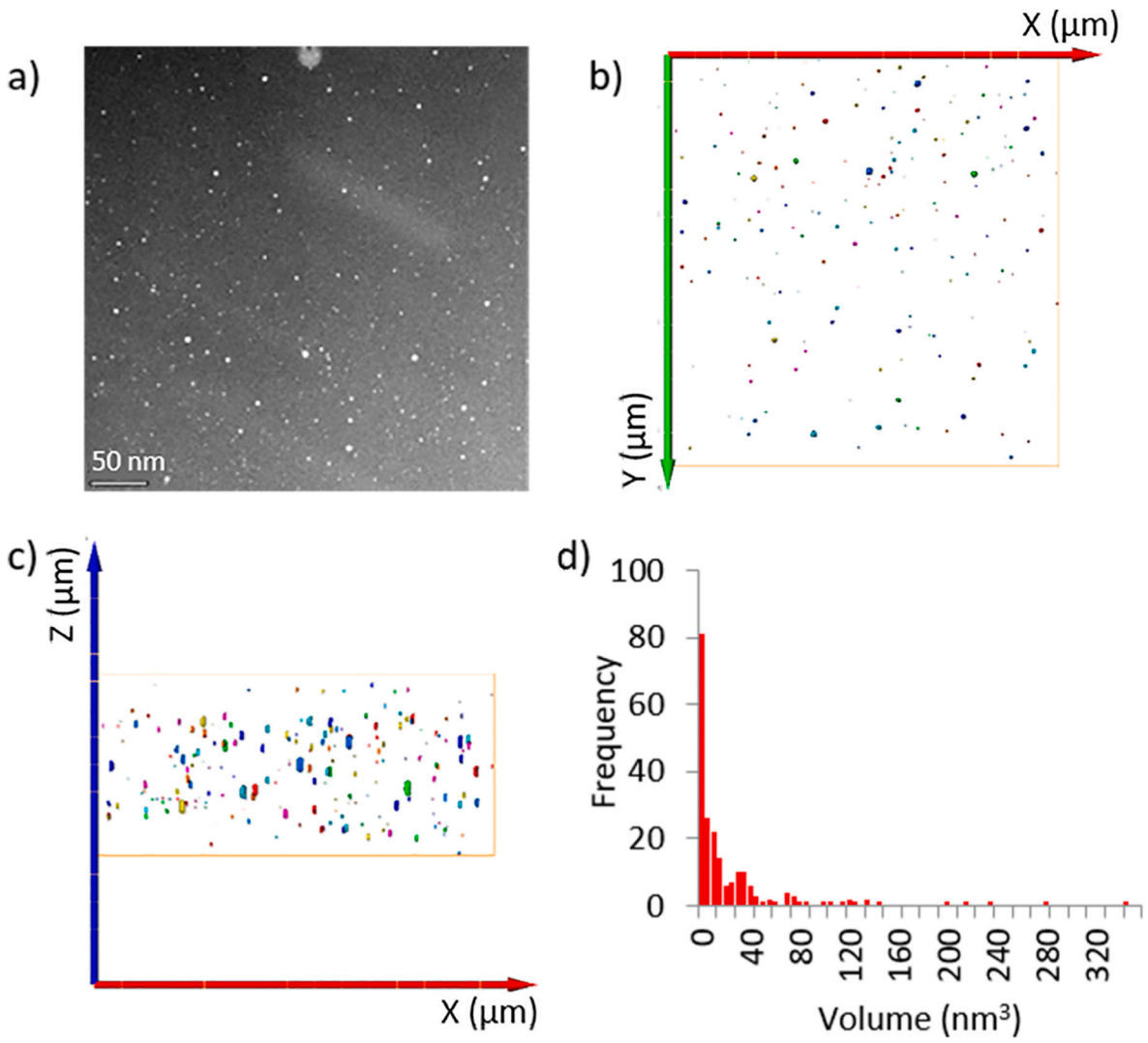

Fig. 6. a) HAADF-STEM image of a nanocomposite of 3 wt% $AgClO_4$ in acrylic resin; b) and c) snapshots obtained from the reconstructed data of an ET analysis of the specimen in a); d) histogram of the size of the Ag NPs.

analysed to obtain better statistics of the NPs distribution. Despite this, the results obtained provide a reasonable view of the structural characteristics of the material. The volume percent of Ag NPs in the acrylic resin has been measured as 0.03% approximately, which accounts for a reduction in the electrical resistivity of four orders of magnitude to 10^{12} Ωcm regarding the pristine resin. Although this is a remarkable result, the percolation threshold for electrical conductivity has not been achieved yet. The analysis of different synthesis parameters such as the addition of increasing amounts of photoinitiator (which activates both the photopolymerization process and the Ag reduction) or the use of different Ag precursors to increase the electrical conductivity is in progress. The correlation between the synthesis conditions, the structural properties of the nanocomposite (analysed by low dose ET) and the electrical resistivity of the material will shed light at the mechanism of electrical conduction in composites, and will allow to achieve advanced conductive nanocomposites with applications in numerous fields.

4. Conclusions

In this work, we provide experimental details to perform low dose ET of acrylic resin based SLA nanocomposites, which allow acquiring 3D structural information to understand and optimize the functional properties of these novel materials. Specimens in the form of nanoneedle are successfully fabricated by FIB, where care should be taken to minimize Ga^+ implantation. An analysis of the effect of the microscope settings in the electron dose is carried out to find optimal low dose conditions to perform the experiments. A phenomenological study of electron beam damage in the material is accomplished, which has evidenced that at very low dose rates the material can withstand large accumulated electron beam doses, allowing the successful acquisition of tilt series of up to 70 images. Two case studies of SLA nanocomposites are shown. The first one consist of WS_2 nanosheets dispersed in the acrylic resin, evidencing that the 3D distribution of the 2D material can be assessed by ET, which is of remarkable importance to understand the basic mechanisms for thermal/electrical conductivity in composites where the percolation threshold is reached. In the second one, our analysis shows that nm-size Ag NPs are formed in-situ during the photopolymerization process by SLA, with a volume percent of 0.03% approximately, which accounts for a reduction in the electrical resistivity of four orders of magnitude to 10^{12} Ωcm regarding the pristine resin.

Author contributions

Conceptualization, M.H. and J.H.-S.; methodology, M.H., J.H.-S and N. F.-D.; validation, M.H., J.H.-S. and N. F.-D.; formal analysis, M.H. and

J.H.-S; investigation, M.H., J.H.-S and L.M.V.; materials preparation: L. M.V.; writing—original draft preparation, M.H.; writing—review and editing, M.H., J.H.-S., L.M.V. and S.I.M.; supervision, M.H.; funding acquisition, M. H. and S.I.M. All authors have read and agreed to the published version of the manuscript.

Declaration of competing interest

The authors declare no conflict of interest.

Data availability

Data will be made available on request.

Acknowledgments

Financial support of Junta de Andalucía under grant PROYEX-CEL_00955 is gratefully acknowledged. Co-funding from UE, Junta de Andalucía (research group INNANOMAT, Ref. TEP946) and UCA (REF. PR2022-008) are also acknowledged. TEM/STEM measurements were carried out at the DME–SC–ICyT-ELECMI-UCA.

Appendix A. Supplementary data

Supplementary data to this article can be found online at https://doi.org/10.1016/j.polymertesting.2023.108232.

References

[1] I. Gibson, D.W. Rosen, B. Stucker, Rapid Prototyping to Direct Digital Manufacturing, 2015. ISBN 9781441911193.
[2] L.J. Kumar, P.M. Pandey, D.I. Wimpenny, 3D Printing and Additive Manufacturing Technologies, Springer Nature Singapore, Singapore, 2019. ISBN 9789811303043.
[3] S.A.M. Tofail, E.P. Koumoulos, A. Bandyopadhyay, S. Bose, L. O'Donoghue, C. Charitidis, Additive manufacturing: scientific and technological challenges, market uptake and opportunities, Mater. Today 21 (2018) 22–37, https://doi.org/10.1016/j.mattod.2017.07.001.
[4] R. D'Aveni, The Pan-Industrial Revolution: How New Manufacturing Titans Will Transform the World, Houghton Mifflin Harcourt, 2018. ISBN 9781328955906.
[5] J. Smit, S. Kreutzer, C. Moeller, M. Carlberg, Industry 4.0 - study for the ITRE committee, Eur. Parliam. (2016) 1–94.
[6] C. Hull, Apparatus for Production of Three-Dimensonal Objects by Stereolithography, 1986, US4575330A.
[7] J.Z. Manapat, Q. Chen, P. Ye, R.C. Advincula, 3D printing of polymer nanocomposites via stereolithography, Macromol. Mater. Eng. 302 (2017) 1–13, https://doi.org/10.1002/mame.201600553.
[8] S.C. Ligon-Auer, M. Schwentenwein, C. Gorsche, J. Stampfl, R. Liska, Toughening of photo-curable polymer networks: a review, Polym. Chem. 7 (2016) 257–286, https://doi.org/10.1039/c5py01631b.
[9] R.D. Farahani, M. Dubé, D. Therriault, Three-Dimensional printing of multifunctional nanocomposites: manufacturing techniques and applications, Adv. Mater. 28 (2016) 5794–5821, https://doi.org/10.1002/adma.201506215.
[10] X. Wang, M. Jiang, Z. Zhou, J. Gou, D. Hui, 3D printing of polymer matrix composites: a review and prospective, Composites, Part B 110 (2017) 442–458, https://doi.org/10.1016/j.compositesb.2016.11.034.
[11] N. Li, S. Huang, G. Zhang, R. Qin, W. Liu, H. Xiong, G. Shi, J. Blackburn, Progress in additive manufacturing on new materials: a review, J. Mater. Sci. Technol. 35 (2019) 242–269, https://doi.org/10.1016/j.jmst.2018.09.002.
[12] H. Wu, W.P. Fahy, S. Kim, H. Kim, N. Zhao, L. Pilato, A. Kafi, S. Bateman, J.H. Koo, Recent developments in polymers/polymer nanocomposites for additive manufacturing, Prog. Mater. Sci. (2020) 111, https://doi.org/10.1016/j.pmatsci.2020.100638.
[13] P.A. Midgley, R.E. Dunin-Borkowski, Electron tomography and holography in materials science, Nat. Mater. 8 (2009) 271–280, https://doi.org/10.1038/nmat2406.
[14] S. Carenco, S. Moldovan, L. Roiban, I. Florea, D. Portehault, K. Vallé, P. Belleville, C. Boissière, L. Rozes, N. Mézailles, et al., The core contribution of transmission electron microscopy to functional nanomaterials engineering, Nanoscale 8 (2016) 1260–1279, https://doi.org/10.1039/c5nr05460e.
[15] Z. Saghi, P.A. Midgley, Electron tomography in the (S)TEM: from nanoscale morphological analysis to 3D atomic imaging, Annu. Rev. Mater. Res. 42 (2012) 59–79, https://doi.org/10.1146/annurev-matsci-070511-155019.
[16] M.C. Scott, C.C. Chen, M. Mecklenburg, C. Zhu, R. Xu, P. Ercius, U. Dahmen, B. C. Regan, J. Miao, Electron tomography at 2.4-ångström resolution, Nature 483 (2012) 444–447, https://doi.org/10.1038/nature10934.
[17] S. Bals, B. Goris, A. De Backer, S. Van Aert, G. Van Tendeloo, Atomic resolution electron tomography, MRS Bull. 41 (2016) 525–530, https://doi.org/10.1557/mrs.2016.138.
[18] W. van Aarle, W.J. Palenstijn, J. De Beenhouwer, T. Altantzis, S. Bals, K. J. Batenburg, J. Sijbers, The ASTRA Toolbox: a platform for advanced algorithm development in electron tomography, Ultramicroscopy 157 (2015) 35–47, https://doi.org/10.1016/j.ultramic.2015.05.002.
[19] C. MessaoudiI, T. Boudier, C.O.S. Sorzano, S.TomoJ. Marco, Tomography software for three-dimensional reconstruction in transmission electron microscopy, BMC Bioinf. 8 (2007) 1–9, https://doi.org/10.1186/1471-2105-8-288.
[20] J.I. Agulleiro, J.J. Fernandez, Tomo3D 2.0 - exploitation of advanced vector eXtensions (AVX) for 3D reconstruction, J. Struct. Biol. 189 (2015) 147–152, https://doi.org/10.1016/j.jsb.2014.11.009.
[21] P.A. Midgley, M. Weyland, 3D electron microscopy in the physical sciences: the development of Z-contrast and EFTEM tomography, Ultramicroscopy 96 (2003) 413–431, https://doi.org/10.1016/S0304-3991(03)00105-0.
[22] D. Wolf, A. Lubk, H. Lichte, H. Friedrich, Towards automated electron holographic tomography for 3D mapping of electrostatic potentials, Ultramicroscopy 110 (2010) 390–399, https://doi.org/10.1016/j.ultramic.2009.12.015.
[23] N. Baba, S. Hata, H. Saito, K. Kaneko, Three-dimensional electron tomography and recent expansion of its applications in materials science, Microscopy 72 (2022) 111–134, https://doi.org/10.1093/jmicro/dfac071.
[24] K.L. Hasezaki, H. Saito, T. Sannomiya, H. Miyazaki, T. Gondo, S. Miyazaki, S. Hata, Three-dimensional visualization of dislocations in a ferromagnetic material by magnetic-field-free electron tomography, Ultramicroscopy 182 (2017) 249–257, https://doi.org/10.1016/j.ultramic.2017.07.016.
[25] R.F. Egerton, Radiation damage to organic and inorganic specimens in the TEM, Micron 119 (2019) 72–87, https://doi.org/10.1016/j.micron.2019.01.005.
[26] H. Vanrompay, A. Béché, J. Verbeeck, S. Bals, Experimental evaluation of undersampling schemes for electron tomography of nanoparticles, Part. Part. Syst. Char. 36 (2019) 1–8, https://doi.org/10.1002/ppsc.201900096.
[27] D. Chen, H. Friedrich, G. De With, On resolution in electron tomography of beam sensitive materials, J. Phys. Chem. C 118 (2014) 1248–1257, https://doi.org/10.1021/jp409185u.
[28] R.F. Egerton, Mechanisms of radiation damage in beam-sensitive specimens , for TEM accelerating voltages between 10 and 300 kV, Microsc. Res. Tech. 75 (2012) 1550–1556, https://doi.org/10.1002/jemt.22099.
[29] Z.J.W.A. Leijten, A.D.A. Keizer, G. De With, H. Friedrich, Quantitative analysis of electron beam damage in organic thin films, J. Phys. Chem. C 121 (2017) 10552–10561, https://doi.org/10.1021/acs.jpcc.7b01749.
[30] B. Kuei, E.D. Gomez, Elucidating mechanisms for electron beam damage in conjugated polymers, Microsc. Microanal. 24 (2018) 1988–1989, https://doi.org/10.1017/s1431927618010425.
[31] P.K. Singh, B.R. Venugopal, D.R. Nandini, Effect of electron beam irradiation on polymers, J. Mod. Mater. 5 (2018) 24–33, https://doi.org/10.1063/1.4710140.
[32] B. Kuei, C. Bator, E.D. Gomez, Imaging 0.36 nm lattice planes in conjugated polymers by minimizing beam damage, Macromolecules 53 (2020) 8296–8302, https://doi.org/10.1021/acs.macromol.0c01082.
[33] J. Ayache, L. Beaunier, J. Boumendil, G. Ehret, D. Laub, Sample Preparation Handbook for Transmission Electron Microscopy, Springer Science + Business Media, Luxembourg, 2010. ISBN 9781441959751.
[34] M.L. Ericson, H. Lindberg, Design and potential of instrumented ultramicrotomy, Polymer (Guildf). 38 (1997) 4485–4489, https://doi.org/10.1016/S0032-3861(96)01051-8.
[35] L.M. Valencia, M. de la Mata, M. Herrera, F.J. Delgado, J. Hernández-Saz, S. I. Molina, Induced damage during STEM-EELS analyses on acrylic-based materials for Stereolithography, Polym. Degrad. Stabil. 203 (2022), 110044, https://doi.org/10.1016/j.polymdegradstab.2022.110044.
[36] P.R. Munroe, The application of focused ion beam microscopy in the material sciences, Mater. Char. 60 (2009) 2–13, https://doi.org/10.1016/j.matchar.2008.11.014.
[37] R.J. Bailey, R. Geurts, D.J. Stokes, F. de Jong, A.H. Barber, Evaluating focused ion beam induced damage in soft materials, Micron 50 (2013) 51–56, https://doi.org/10.1016/j.micron.2013.04.005.
[38] S. Kim, M. Jeong Park, N.P. Balsara, G. Liu, A.M. Minor, Minimization of focused ion beam damage in nanostructured polymer thin films, Ultramicroscopy 111 (2011) 191–199, https://doi.org/10.1016/j.ultramic.2010.11.027.
[39] J.F. Ziegler, M.D. Ziegler, J.P. Biersack, Srim - the stopping and range of ions in matter, Nucl. Instrum. Methods Phys. Res. Sect. B Beam Interact. Mater. Atoms 268 (2010) 1818–1823, https://doi.org/10.1016/j.nimb.2010.02.091, 2010.
[40] X. Chu, H. Heidari, A. Abelson, D. Unruh, C. Hansen, C. Qian, G. Zimanyi, M. Law, A.J. Moulé, Structural characterization of a polycrystalline epitaxially-fused colloidal quantum dot superlattice by electron tomography, J. Mater. Chem. A 8 (2020) 18254–18265, https://doi.org/10.1039/d0ta06704k.
[41] L. Nicolai, K. Biermann, A. Trampert, Application of electron tomography for comprehensive determination of III-V interface properties, Ultramicroscopy 224 (2021), 113261, https://doi.org/10.1016/j.ultramic.2021.113261.
[42] S. Ndiaye, S. Duguay, F. Vurpillot, C. Carraro, G. Maggioni, E. Di Russo, D. De Salvador, E. Napolitani, L. Rigutti, Atom probe tomography of hyper-doped Ge layers synthesized by Sb in-diffusion by pulsed laser melting, Mater. Sci. Semicond. Process. 164 (2023), 107641, https://doi.org/10.1016/j.mssp.2023.107641.
[43] R. Wu, Y. Yu, S. Jia, C. Zhou, O. Cojocaru-Mirédin, M. Wuttig, Strong charge carrier scattering at grain boundaries of PbTe caused by the collapse of metavalent bonding, Nat. Commun. (2023) 14, https://doi.org/10.1038/s41467-023-36415-1.

[44] J. Hernández-Saz, M. Herrera, S.I. Molina, A methodology for the fabrication by FIB of needle-shape specimens around sub-surface features at the nanometre scale, Micron 43 (2012) 643–650, https://doi.org/10.1016/j.micron.2011.11.011.
[45] Q. Chen, C. Dwyer, G. Sheng, C. Zhu, X. Li, C. Zheng, Y. Zhu, Imaging beam-sensitive materials by electron microscopy, Adv. Mater. 32 (2020) 1–42, https://doi.org/10.1002/adma.201907619.
[46] E. Bladt, D.M. Pelt, S. Bals, K.J. Batenburg, Electron tomography based on highly limited data using a neural network reconstruction technique, Ultramicroscopy 158 (2015) 81–88, https://doi.org/10.1016/j.ultramic.2015.07.001.
[47] W. Albrecht, S. Bals, Fast electron tomography for nanomaterials, J. Phys. Chem. C 124 (2020) 27276–27286, https://doi.org/10.1021/acs.jpcc.0c08939.
[48] H. Vanrompay, A. Skorikov, E. Bladt, A. Béché, B. Freitag, J. Verbeeck, S. Bals, Fast versus conventional HAADF-STEM tomography of nanoparticles: advantages and challenges, Ultramicroscopy (2021) 221, https://doi.org/10.1016/j.ultramic.2020.113191.
[49] S. Koneti, L. Roiban, F. Dalmas, C. Langlois, A.S. Gay, A. Cabiac, T. Grenier, H. Banjak, V. Maxim, T. Epicier, Fast electron tomography: applications to beam sensitive samples and in situ TEM or operando environmental TEM studies, Mater. Char. 151 (2019) 480–495, https://doi.org/10.1016/j.matchar.2019.02.009.
[50] E.A. Stach, J. Li, H. Xin, D. Zakharov, Y.H. Kwon, E. Reichmanis, Combining post-specimen aberration correction and direct electron detection to image molecular structure in liquid crystal polymers, Microsc. Microanal. 22 (2016) 1924–1925, https://doi.org/10.1017/s1431927616010461.
[51] S. Juhl, X. Li, J. Badding, N. Alem, Monochromated low-dose aberration-corrected transmission electron microscopy of diamondoid carbon nanothreads, Microsc. Microanal. 22 (2016) 1840–1841, https://doi.org/10.1017/s1431927616010047.
[52] L.M. Valencia, M. Herrera, F.J. Delgado, S.I. Molina, P. Degradation, M. Herrera, F. J. Delgado, S.I. Molina, P. Degradation, Induced damage during STEM-EELS analyses on acrylic-based materials for stereolithography, Polym. Degrad. Stabil. (2022), https://doi.org/10.1016/j.polymdegradstab.2022.110044.
[53] M. Nord, P. Erik, I. Hallsteinsen, T. Tybell, R. Holmestad, Assessing electron beam sensitivity for SrTiO3 and La0.7Sr0.3MnO3 using electron energy loss spectroscopy, Ultramicroscopy 169 (2016) 98–106, https://doi.org/10.1016/j.ultramic.2016.07.004.
[54] B.E. Bammes, J. Jakana, M.F. Schmid, W. Chiu, Radiation damage effects at four specimen temperatures from 4 to 100 K, J. Struct. Biol. 169 (2010) 331–341, https://doi.org/10.1016/j.jsb.2009.11.001.
[55] J.P. Buban, Q. Ramasse, B. Gipson, N.D. Browning, H. Stahlberg, High-resolution low-dose scanning transmission electron microscopy, J. Electron. Microsc. 59 (2010) 103–112, https://doi.org/10.1093/jmicro/dfp052.
[56] C. Guo, F.I. Allen, Y. Lee, T.P. Le, C. Song, J. Ciston, A.M. Minor, E.D. Gomez, Probing local electronic transitions in organic semiconductors through energy-loss spectrum imaging in the transmission electron microscope, Adv. Funct. Mater. 25 (2015) 6071–6076, https://doi.org/10.1002/adfm.201502090.
[57] K. Siangchaew, M. Libera, The influence of fast secondary electrons on the aromatic structure of polystyrene, Philos. Mag. A Phys. Condens. Matter, Struct. Defects Mech. Prop. 80 (2000) 1001–1016, https://doi.org/10.1080/01418610008212095.
[58] B. Kuei, E.D. Gomez, Pushing the limits of high-resolution polymer microscopy using antioxidants, Nat. Commun. 12 (2021) 153, https://doi.org/10.1038/s41467-020-20363-1.
[59] M.B. Braunfeld, A.J. Koster, J.W. Sedat, D.A. Agard, Cryo automated electron tomography: towards high-resolution reconstructions of plastic-embedded structures, J. Microsc. 174 (1994) 75–84, https://doi.org/10.1111/j.1365-2818.1994.tb03451.x.
[60] C. Drevelle, S. Duquesne, M. Le Bras, J. Lefebvre, R. Delobel, A. Castrovinci, C. Magniez, M. Vouters, Influence of ammonium polyphosphate on the mechanism of thermal degradation of an acrylic binder resin, J. Appl. Polym. Sci. 94 (2004) 717–729, https://doi.org/10.1002/app.20868.
[61] J.K. Chen, F.H. Ko, F.C. Chang, Structural transformation of acrylic resin upon controlled electron-beam exposure yields positive and negative resists, Adv. Funct. Mater. 15 (2005) 1147–1154, https://doi.org/10.1002/adfm.200400077.
[62] J.R. Fryer, Radiation damage in organic crystalline films, Ultramicroscopy 14 (1984) 227–236, https://doi.org/10.1016/0304-3991(84)90091-3.
[63] N. Jiang, J.C.H. Spence, On the dose-rate threshold of beam damage in TEM, Ultramicroscopy 113 (2012) 77–82, https://doi.org/10.1016/j.ultramic.2011.11.016.
[64] R.F. Egerton, I. Rauf, Dose-rate dependence of electron-induced mass loss from organic specimens, Ultramicroscopy 80 (1999) 247–254, https://doi.org/10.1016/S0304-3991(99)00114-X.
[65] S. Yakovlev, M. Libera, Dose-limited spectroscopic imaging of soft materials by low-loss EELS in the scanning transmission electron microscope, Micron 39 (2008) 734–740, https://doi.org/10.1016/j.micron.2007.10.019.
[66] K. Varlot, J.M. Martin, C. Quet, EELS analysis of PMMA at high spatial resolution, Micron 32 (2001) 371–378, https://doi.org/10.1016/S0968-4328(00)00017-2.
[67] R.F. Egerton, Control of radiation damage in the TEM, Ultramicroscopy 127 (2013) 100–108, https://doi.org/10.1016/j.ultramic.2012.07.006.
[68] L.R. Parent, E. Bakalis, M. Proetto, Y. Li, C. Park, F. Zerbetto, N.C. Gianneschi, Tackling the challenges of dynamic experiments using liquid-cell transmission electron microscopy, Acc. Chem. Res. 51 (2018) 3–11, https://doi.org/10.1021/acs.accounts.7b00331.
[69] M. Zhang, R.C.T. Howe, R.I. Woodward, E.J.R. Kelleher, F. Torrisi, G. Hu, S. V. Popov, J.R. Taylor, T. Hasan, Solution processed MoS2-PVA composite for sub-bandgap mode-locking of a wideband tunable ultrafast Er:fiber laser, Nano Res. 8 (2015) 1522–1534, https://doi.org/10.1007/s12274-014-0637-2.
[70] Z. Luo, Y. Li, M. Zhong, Y. Huang, X. Wan, J. Peng, J. Weng, Nonlinear optical absorption of few-layer molybdenum diselenide (MoSe_2) for passively mode-locked soliton fiber laser [Invited], Photon. Res. 3 (2015) A79, https://doi.org/10.1364/prj.3.000a79.
[71] A. Sorrentino, C. Altavilla, M. Merola, A. Senatore, P. Ciambelli, S. Iannace, Nanosheets of MoS2-oleylamine as hybrid filler for self-lubricating polymer composites: thermal, tribological and mechanical properties, Polym. Compos. 36 (2015) 1124–1134, https://doi.org/10.1002/pc.23444.
[72] K. Zhou, S. Jiang, C. Bao, L. Song, B. Wang, G. Tang, Y. Hu, Z. Gui, Preparation of poly(vinyl alcohol) nanocomposites with molybdenum disulfide (MoS 2): structural characteristics and markedly enhanced properties, RSC Adv. 2 (2012) 11695–11703, https://doi.org/10.1039/c2ra21719h.
[73] O. Eksik, J. Gao, S.A. Shojaee, A. Thomas, P. Chow, S.F. Bartolucci, D.A. Lucca, N. Koratkar, Epoxy nanocomposites with two-dimensional transition metal dichalcogenide additives, ACS Nano 8 (2014) 5282–5289, https://doi.org/10.1021/nn5014098.
[74] C. Zhi, Y. Bando, C. Tang, H. Kuwahara, D. Golberg, Large-scale fabrication of boron nitride nanosheets and their utilization in polymeric composites with improved thermal and mechanical properties, Adv. Mater. 21 (2009) 2889–2893, https://doi.org/10.1002/adma.200900323.
[75] D. Zhang, T. Liu, J. Cheng, S. Liang, J. Chai, X. Yang, H. Wang, G. Zheng, M. Cao, Controllable synthesis and characterization of tungsten disulfide nanosheets as promising nanomaterials for electronic devices, Ceram. Int. 45 (2019) 12443–12448, https://doi.org/10.1016/j.ceramint.2019.03.177.
[76] A. Mojtabaei, M. Otadi, V. Goodarzi, H.A. Khonakdar, S.H. Jafari, U. Reuter, U. Wagenknecht, Influence of fullerene-like tungsten disulfide (IF-WS2) nanoparticles on thermal and dynamic mechanical properties of PP/EVA blends: correlation with microstructure, Composites, Part B 111 (2017) 74–82, https://doi.org/10.1016/j.compositesb.2016.12.006.
[77] S. Manjunatha, T. Machappa, A. Sunilkumar, Y.T. Ravikiran, Tungsten disulfide: an efficient material in enhancement of AC conductivity and dielectric properties of polyaniline, J. Mater. Sci. Mater. Electron. 29 (2018) 11581–11590, https://doi.org/10.1007/s10854-018-9255-1.
[78] P. Martínez-Merino, A. Sánchez-Coronilla, R. Alcántara, E.I. Martín, I. Carrillo-Berdugo, R. Gómez-Villarejo, J. Navas, The role of the interactions at the tungsten disulphide surface in the stability and enhanced thermal properties of nanofluids with application in solar thermal energy, Nanomaterials 10 (2020), https://doi.org/10.3390/nano10050970.
[79] M. Sahu, L. Narashimhan, O. Prakash, A.M. Raichur, Noncovalently functionalized tungsten disulfide nanosheets for enhanced mechanical and thermal properties of epoxy nanocomposites, ACS Appl. Mater. Interfaces 9 (2017) 14347–14357, https://doi.org/10.1021/acsami.7b01608.
[80] J. Loos, E. Sourty, K. Lu, B. Freitag, D. Tang, D. Wall, Electron tomography on micrometer-thick specimens with nanometer resolution, Nano Lett. 9 (2009) 1704–1708, https://doi.org/10.1021/nl900395g.
[81] A.J. Fijneman, M. Goudzwaard, A.D.A. Keizer, P.H.H. Bomans, T. Gebäck, M. Palmlöf, M. Persson, J. Högblom, G. de With, H. Friedrich, Local quantification of mesoporous silica microspheres using multiscale electron tomography and lattice Boltzmann simulations, Microporous Mesoporous Mater. (2020) 302, https://doi.org/10.1016/j.micromeso.2020.110243.
[82] K. Gnanasekaran, G. de With, H. Friedrich, Quantification and optimization of ADF-STEM image contrast for beam-sensitive materials, R. Soc. Open Sci. 5 (2018), https://doi.org/10.1098/rsos.171838.
[83] L.M. Valencia, M. Herrera, M. de la Mata, A.S. de León, F.J. Delgado, S.I. Molina, Synthesis of silver nanocomposites for stereolithography: in situ formation of nanoparticles, Polymers 14 (2022), https://doi.org/10.3390/polym14061168.
[84] L.M. Valencia, M. Herrera, M. de la Mata, J. Hernández-Saz, I. Romero-Ocaña, F. J. Delgado, J. Benito, S.I. Molina, Stereolithography of semiconductor silver and acrylic-based nanocomposites, Polymers 14 (2022), https://doi.org/10.3390/polym14235238.